



Exploration of the Interplay of Dissipation and Disorder with Tensor Network Methods

Bachelor's Thesis submitted

to

Prof. Dr. Jens Eisert

Freie Universität Berlin

by

Leon Immanuel Klein

(4753165)

in partial fulfillment of the requirements

for the degree of

Bachelor of Science

Berlin, December 16, 2016

Acknowledgement

I would like to thank Prof. Dr. Jens Eisert for making this work possible and also for providing useful insights during the work process.

I am also grateful to Dr. Albert H. Werner who helped me throughout on the work of this thesis. He also provided the necessary code for the simulations and helped me use it.

Moreover, I would like to thank Christian Krumnow for his constant and helpful advice.

Abstract

Transport properties of quantum many-body systems have been at the center of research in condensed matter physics for many years. Moreover, the investigation of the impact of disorder and dissipation on localisation and transport effects is an active research field. Recent experiments were able to directly observe and investigate the expected breakdown of particle transport due to disorder in controlled environments and the loss of coherence due to dissipation which results in a loss of localisation. Motivated by that we perform simulations using tensor network methods for open quantum many-body systems in order to study the impact of dissipation on localised interacting quantum many-body systems. This is done for different kinds of systems and interactions with the environment. We probe the localisation properties of the system by studying the persistence of particle number imbalances over time. We show that disorder in uncoupled systems leads to localisation effects dependent on the disorder strength. The presence of couplings to the environment leads to destruction of this localisation effect, the time scale of this is governed by the interaction strength with the environment.

Contents

Introduction	1
1 Theory	2
1.1 Quantum many-body systems	2
1.2 Matrix product states (MPS)	3
1.2.1 Notation	3
1.2.2 Definition of matrix product states	4
1.2.3 Interlude: Area Laws	5
1.3 Matrix-product operators (MPO)	6
1.4 Time evolution of mixed states	7
1.4.1 Trotter-Suzuki expansion	9
1.4.2 Applying the different time evolution layers	10
1.4.3 Calculating expectation values	11
2 Many-body localisation	14
2.1 Anderson localisation	14
2.2 Many-body localisation	15
2.3 Experimental observation of many-body localisation	15
3 Simulation and results	18
3.1 Realisations	18
3.2 Spinless fermionic chain	19
3.2.1 Setting	19
3.2.2 Dissipation	21
3.2.3 Results of the spinless isolated fermionic chain	21
3.2.4 Results of the spinless fermionic chain with dephasing	22
3.2.5 Spinless fermionic chain with particle loss	25
3.3 Spinful fermionic chain	27
4 Conclusion	30
A Statistic for the disorder simulations	33
B Simulation errors	33
C Dependence of particle loss on the coupling strength	36

Introduction

The investigation of transport of quantum many-body systems is one of the most active fields in condensed matter physics [1]. Especially the impact of disorder and dissipation on transport has been at the center of research. Furthermore, these questions are relevant both from a foundational as well as from an applied point of view. Already more than 50 years ago, Anderson found localisation effects due to disorder and therefore the breakdown of any transport for non interacting isolated one-dimensional systems [2]. Hence such a system would fail to thermalise and be an insulator. Particles in real systems however, do interact to some extent with each other and the environment. Therefore, in recent years the stability of Anderson localisation in interacting many-body systems has become an important research field. Experimental ([3],[4]) as well as theoretical studies ([5],[6],[7],[8]) observed similarities to Anderson localisation for interacting many-body systems in respect to particle transport, although the particle transport does not break down in every case [5]. In contrast to Anderson localisation however, the correlation between different parts of the system can grow without bound albeit slowly in time, which enables information transport [8]. However, it is not yet clear if these localised systems fail to thermalise or reach their equilibrium just after a very long time [6]. Furthermore, all real systems interact to some extent with their surroundings, which reduces the coherence needed for localisation. Accordingly, another important and interesting question is how these localised systems behave under influences from their surroundings, which will be one of the key questions in this thesis. We will approach this problem with the help of tensor networks [9], which have proven to be a good ansatz class to describe systems with bounded correlations.

The rest of the thesis is organised as follows: In the first chapter quantum many-body systems and matrix product states are introduced. Moreover, the time evolution of open systems is discussed based on tensor networks. In the second chapter, we have a look at many-body localisation and recent experiments which investigate this behaviour. In the third chapter the investigated fermionic systems are described. After that, the parameters and the results of the simulations are presented and discussed.

1 Theory

The information for the following summary of many-body systems (1.1) and matrix product states (1.2) is taken from the lecture notes *Entanglement and tensor network states* by Jens Eisert [10] and from the book *Quantum Computation and Quantum Information* [11]. The second part of the theory discussing Matrix product operators and the time evolution of open systems (starting from 1.3) is based on a paper by Werner et al. [9]. The theoretical operations are explained based on the code we use for our simulations and which is also explained in the paper.

1.1 Quantum many-body systems

A state of finite dimensional quantum systems is described by a vector in a Hilbert space \mathcal{H} . In condensed matter, many of these systems form a so called *quantum many-body system*. In particular, the internal interplays of these system are of mayor physical interest. In this thesis we will focus on one-dimensional quantum many-body systems which have a finite lattice structure of N sites, whereby each site i has an internal degree of freedom of dimension d . This could be a system of N distinguishable particles with a spin degree of freedom of the dimension $d = 2$. A picture of such a chain can be seen in figure 1. Each local quantum system with an internal degree of freedom d can be described by a Hilbert space $\mathcal{H} = (\mathbb{C}^d)$. The basis of such a Hilbert space can be denoted as $|j\rangle$ with $j \in \{1, \dots, d\}$. Let us now look at a compound system of N distinguishable systems $i \in \{1, \dots, N\}$ with a local internal degree of freedom of dimension d each. The whole Hilbert space \mathcal{H} of the system is given by the tensor product of all local Hilbert spaces \mathcal{H}_i

$$\mathcal{H} = \mathcal{H}_1 \otimes \mathcal{H}_2 \otimes \dots \otimes \mathcal{H}_N. \quad (1)$$

A basis vector of this Hilbert space \mathcal{H} is given by the product basis of each local system i connected with the tensor product

$$|j_1\rangle \otimes |j_2\rangle \otimes \dots \otimes |j_N\rangle = |j_1, j_2, \dots, j_N\rangle, \quad (2)$$

with $j_i \in \{1, \dots, d\}$. This means any state $|\psi\rangle \in \mathcal{H}$ can be written as

$$|\psi\rangle = \sum_{j_1, j_2, \dots, j_N=1}^d c_{j_1, j_2, \dots, j_N} |j_1, j_2, \dots, j_N\rangle, \quad (3)$$

where $c_{j_1, j_2, \dots, j_N} \in \mathbb{C}$ are the associated coefficients of the basis vectors. As seen in equation 3, one needs d^N coefficients to describe all possible states. Therefore, the Hilbert space has

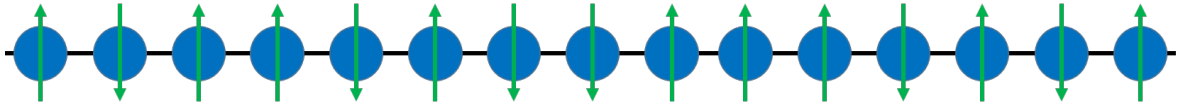


Figure 1: One-dimensional particle chain with a local internal spin degree of freedom of dimension $d = 2$.

dimension d^N and already the description of small systems can be difficult. For example, a spin chain with a spin degree of freedom of dimension $d = 2$ and $N = 32$ particles would need $2^{32} \times 2 \times 8\text{B} = 64\text{GB}$ disc space for double precision of complex entries. Moreover, the computational cost of typical numeric operations, like matrix multiplications, scales at least quadratic with the system size N where numerical methods quickly reach their limits. Therefore, numerical methods must restrict to smaller subsets of the Hilbert space which then approximates some states of a system in the whole Hilbert space. Desired properties of these subsets are that they give a reasonable approximation to physically relevant states and that they are efficient in terms of numerical operation costs and storage. It turns out that a very powerful method is given by the decomposition of the coefficient tensor which is developed in the next section.

1.2 Matrix product states (MPS)

A tensor T maps a set of input vectors multilinearly to a value. Equivalently a tensor can be described with a multidimensional array $T \in \mathbb{C}^{d_1} \otimes \mathbb{C}^{d_2} \otimes \dots \otimes \mathbb{C}^{d_o}$ with the entries $T_{\alpha_1, \dots, \alpha_o}$ with $\alpha_i \in \{1, \dots, d_i\}$, whereby the number of vector spaces o is called the *order* of T .

1.2.1 Notation

In the following we use a graphical notation to work with tensors. In this notation, a tensor is represented by a box with edges, where each edge corresponds with one free index of the tensor. Therefore a scalar has no edges and for example a matrix two (see figure 2a and b). These edges can be also used to connect the tensors. This represents the *contraction of indices*, meaning that we sum two corresponding indices of two tensors over the same summation index. An example for this is a matrix product of two matrices $A \in \mathbb{C}^{m \times n}$ and $B \in \mathbb{C}^{n \times l}$

$$(AB)_{ik} = \sum_{j=1}^n A_{ij} B_{jk} = C_{ik}, \quad (4)$$

which is represented by connecting the two corresponding edges together (see figure 2c). A system of such connected tensors is called a *tensor network*. Different forms of tensor networks



Figure 2: Graphical notation of different tensors. The number of edges represents the order of the tensor. **a)** Shows a scalar. **b)** Shows a matrix and therefore has two edges. **c)** Shows matrix product of two matrices $A \in \mathbb{C}^{m \times n}$ and $B \in \mathbb{C}^{n \times l}$. Resulting again in a matrix.

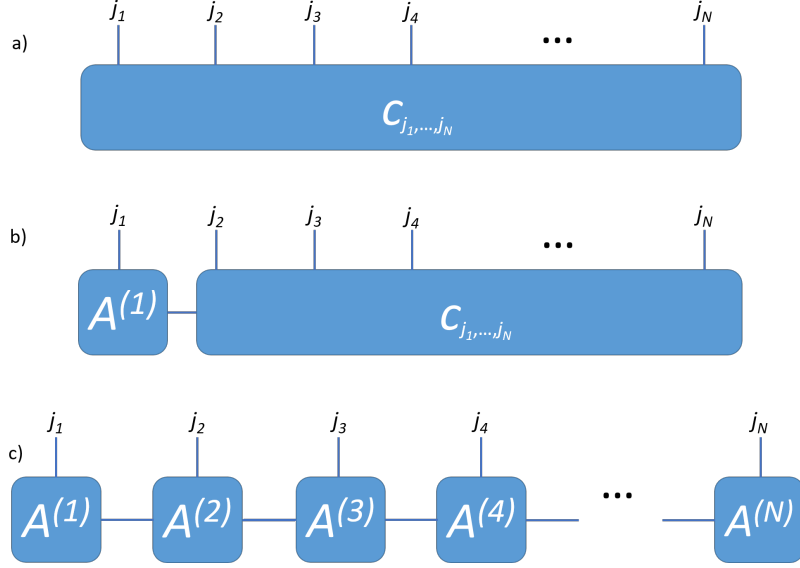


Figure 3: Representation of the coefficient tensor of a state $|\psi\rangle$ described in equation 3: **a)** in the graphical notation and therefore as a box with N edges. This tensor can be deposited into a tensor network. **b)** The first singular value decomposition splits a tensor $A^{(1)}$ from the coefficient tensor. **c)** After all decompositions as a *matrix product state*. Each tensor $A^{(i)}$ has the form $\mathbb{C}^{D \times D \times d}$. The edges represent the connection between the tensors.

can be seen in figure 3 which is explained later. For complex tensor networks the order of contractions can make a big difference in the calculation cost. In the next step we will use tensor networks to obtain a set of efficiently describable states which are physically relevant.

1.2.2 Definition of matrix product states

Let us return to a state $|\psi\rangle \in \mathcal{H}$ described in equation 3. The coefficients c_{j_1, j_2, \dots, j_N} of this state can be represented by a tensor (see figure 3a). This coefficient tensor has N edges, for each physical dimension one and d^N entries. The goal is to find a decomposition of this coefficient tensor, which is compatible with the localisation structure of natural physical systems. Therefore we decompose the tensor into multiple tensors, one for each site. This

can be done with singular value decompositions.

Singular value decomposition (SVD) Every matrix A of dimensions $(m \times n)$ can be decomposed via a *singular value decomposition* (SVD) to

$$A = USV^\dagger, \quad (5)$$

whereby U is a unitary matrix with the dimensions $(m \times m)$. S is a diagonal matrix of the rank $r = (\min(n, m))$ and the dimensions $(m \times n)$. All entries are positive and called *singular values*. V^\dagger is of the dimension $(n \times n)$ and also unitary [12].

We start by merging all physical dimensions besides the first one together, because SVD are only possible for matrices. Then we perform the SVD and the products are a unitary tensor U for the first site and a tensor SV^\dagger for the rest (see figure 3b). This process is then repeated for the other sites. It is possible to decompose any coefficient tensor in this way [13]. The result of this is a matrix product of tensors $A^{(i)}$ of order three (see figure 3c). Therefore, the coefficients of the state $|\psi\rangle$ can be also written as

$$c_{j_1, j_2, \dots, j_N} = \sum_{\alpha}^{D_1} \sum_{\beta}^{D_2} \dots \sum_{\omega}^{D_N} A_{\alpha; j_1}^{(1)} A_{\alpha, \beta; j_2}^{(2)} \dots A_{\omega; j_N}^{(N)} = A_{j_1}^{(1)} A_{j_2}^{(2)} \dots A_{j_N}^{(N)}, \quad (6)$$

where only the virtual indices of each *bond dimensions* D_i are contracted and the physical indices j_i are left open. In this case the maximal bond dimension $D = \max(D_1, D_2, \dots, D_N)$ has to be of the size $d^{N/2}$, due to the SVD. Here we use open boundary conditions. Therefore the first $A_{j_1}^{(1)}$ and the last tensor $A_{j_N}^{(N)}$ in the MPS are of the form $\mathbb{C}^{1 \times D_1 \times d}$ and $\mathbb{C}^{D_N \times 1 \times d}$. All other tensors have the form $\mathbb{C}^{D_i \times D_{i+1} \times d}$. Therefore, maximal $O(NdD^2)$ parameters are needed in this case, but the maximal bond dimension D scales exponentially with N . Every state can be written in this MPS description. To reduce the number of required parameters one can set a limit to the bond dimension, which still allows, a good approximation of a lot of certain states.

1.2.3 Interlude: Area Laws

Let us look at any generic state in the Hilbert space $\mathcal{H} = (\mathbb{C}^d)^{\otimes N}$. Most states living in the Hilbert space fulfil a volume law, meaning that the entanglement between any subsystem A of the state and its complement B is scaling with the size of the subsystem. However, it can be proven that MPS for one-dimensional systems with a limit for the bond dimension satisfy an area law, meaning that the entanglement is scaling only with the size of the boundaries. Therefore these MPS only allow the description of certain correlations. But there are also

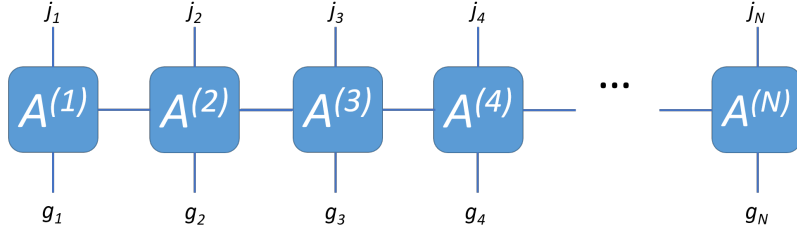


Figure 4: The decomposed coefficient tensor of a mixed state described in equation 8, called *matrix-product operator*. The picture is similar to the one of a matrix-product state (see figure 3b).

natural occurring states which are proven to fulfil an area law, like a non degenerated ground state with an energy gap or product states [14]. In fact most naturally occurring states seem to fulfil an area law, making them occupy only a small fraction of the whole possible Hilbert space \mathcal{H} [15]. This makes MPS a reasonable and powerful class to describe a lot of naturally occurring states and motivates further the restriction to the bond dimension.

1.3 Matrix-product operators (MPO)

MPS as described above only capture pure states, but mixed states can also be described by similar tensor networks. These are called *matrix-product operators (MPO)*. The state is now captured by a density matrix. This gives the description of the mixed state

$$\rho = \sum_{j_1, \dots, j_N=1}^d \sum_{g_1, \dots, g_N=1}^d p_{j_1, \dots, j_N, g_1, \dots, g_N} |j_1, \dots, j_N\rangle \langle g_1, \dots, g_N|, \quad (7)$$

with the coefficients $p_{j_1, \dots, j_N, g_1, \dots, g_N} \in \mathbb{C}$. The coefficient tensor can again be decomposed by SVD similar to the MPS case (see figure 4). Therefore the coefficients can again be written in a similar way to equation 6, but now each tensor $A_{j_i, g_i}^{(i)}$ has two physical edges instead of one. Therefore the MPO of this state can be written as

$$\rho = \sum_{j_1, \dots, j_N=1}^d \sum_{g_1, \dots, g_N=1}^d A_{j_1, g_1}^{(1)} \dots A_{j_N, g_N}^{(N)} |j_1, \dots, j_N\rangle \langle g_1, \dots, g_N|. \quad (8)$$

The maximal bond dimension D between two tensors $A_{j_i, g_i}^{(i)}$ can be again restricted. An important property of a density operator is the positivity, meaning that all eigenvalues are positive. It is hard to test for this property in the MPO description, but the positivity is guaranteed if we describe the density matrix ρ in its purified form. The purified form is given by $\rho = XX^\dagger$ with the purification operator X described by a tensor network

$$X_{j_1, \dots, j_N, \kappa_1, \dots, \kappa_N} = \sum_{\alpha}^{D_1} \sum_{\beta}^{D_2} \dots \sum_{\omega}^{D_N} A_{\alpha; \kappa_1; j_1}^{(1)} A_{\alpha, \beta; \kappa_2; j_2}^{(2)} \dots A_{\omega; \kappa_N; j_N}^{(N)}, \quad (9)$$

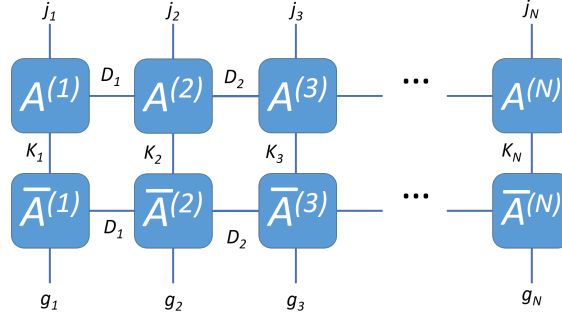


Figure 5: Notation for the coefficient tensor of the (mixed) state ρ in its purified form captured by two connected tensor networks. For each site there is a tensor $A^{(i)}$ and its adjoint counterpart $\bar{A}^{(i)}$. These are connected by the Kraus dimension K_i . The connection to the neighbouring tensors is the bond dimension D_i . The open physical indices of dimension d are denoted as usual with j_i and g_i .

whereby j_i denotes the index of the physical dimensions and κ_i the index of the *Kraus dimension* K_i of the tensor $A^{(i)}$ for site i [9]. The Kraus dimension also connects the two layers X and X^\dagger of the purified form (see figure 5).

1.4 Time evolution of mixed states

The main assumption in quantum mechanics is that we have a unitary time evolution which is generated by Hamiltonians. However, such a unitary time evolution holds only true for isolated systems. In a realistic context no system is completely isolated from its surroundings. Hence one would have to perform the time evolution for the whole universe in order to perform the time evolution for any real system. None the less in many situations we can approximate the influences of the environment with the interaction of our system with a heat bath. In this Markovian approximation the changes in the surroundings are fast and therefore all changes due to interaction with our system equilibrate very fast compared to the evolution in our system. This means the surrounding has no memory and is approximated as an infinite bath. Therefore the Hamiltonian H acts exclusively on our system and the effective time evolution of the interactions with the environment is approximated by a completely positive semi group [16]. The corresponding time evolution for the density matrix ρ is given by the Lindblad master equation

$$\frac{d\rho}{dt} = \mathcal{L}(\rho) = -i[H, \rho] + \mathcal{D}(\rho), \quad (10)$$

whereby H is the Hamiltonian of the system and \mathcal{D} describes the dissipative part of the system and is given by

$$\mathcal{D}(\rho) = \sum_l (L_l \rho L_l^\dagger - \frac{1}{2} \{L_l^\dagger L_l, \rho\}), \quad (11)$$

where the summation over l runs over all different used Lindblad operators which are further explained in 3.2.2 on page 21. Since the action from \mathcal{L} on ρ is linear, we can find a matrix representation of the vector $e^{\tau\mathcal{L}}$ on the vector space of matrices. Concretely we can choose $|i\rangle\langle j| \mapsto |i\rangle|j\rangle$, a row-wise vectorisation. This mapping implies for left and right matrix multiplications the following identity

$$|AXB\rangle = (A \otimes B^T) |X\rangle. \quad (12)$$

In this picture the integration of the Lindblad master equation is given by

$$|\rho_{t+\tau}\rangle = e^{\tau\mathcal{L}}(\rho_t) = e^{\tau(-iH \otimes \mathbb{1} + i\mathbb{1} \otimes \overline{H} + \mathcal{D})}(|\rho_t\rangle), \quad (13)$$

whereby $|\rho_{t+\tau}\rangle$ denotes in this case the row-wise concatenation of the density matrix ρ [9].

The Hamiltonians H we use in this thesis can be split into local acting parts:

$$H = \sum_{i=1}^N h^{(i)}, \quad (14)$$

where $h^{(i)}$ is at most supported on two sites. These are commonly used Hamiltonians, because they represent the locality in condensed matter well. Moreover, systems on which these kind of Hamiltonians act can be studied in the laboratory, allowing the simulation of systems which can not be simulated yet on ordinary computers. An example for such an experiment are cold atoms in an optical lattice which will be discussed later (see section 2.3 on page 15). These Hamiltonians have the nice property that the terms can be arranged in an even layer H_e and an odd one H_o . The even layer contains all the terms which act on an even second site i and the odd one contains the rest. Each layer consists of mutual commuting terms, because they act on different sites. Because of this the unitary time evolution of the density matrix $\rho = XX^\dagger$ can be written as

$$\rho(t) = U_e U_o \rho U_o^\dagger U_e^\dagger = U_e U_o X X^\dagger U_o^\dagger U_e^\dagger = U_e U_o X (U_e U_o X)^\dagger, \quad (15)$$

where U_e and U_o are the unitary time evolution operators of the two layers. As seen in this equation it is enough to perform the time evolution just for one part of the purified form $X \mapsto U_e U_o X$, because the other can be achieved by taking the adjoint. This stresses again the usefulness of the purified form.

Each Lindblad-operator acts only on a single site and therefore we can write $e^{\tau\mathcal{D}} = e^{\tau\mathcal{D}^{(1)}} \otimes \dots \otimes e^{\tau\mathcal{D}^{(N)}}$. Hence the dissipative part computes to

$$\mathcal{D}(\rho) = \sum_i \sum_l (L_l^{(i)} \rho L_l^{(i)\dagger} - \frac{1}{2} \{L_l^{(i)\dagger} L_l^{(i)}, \rho\}), \quad (16)$$

where the first sum runs over all sites i on which each local Lindblad-operator $L_l^{(i)}$ acts. Moreover, because $e^{\tau\mathcal{D}^{(i)}}$ is completely positive one can find so called *Kraus operators* $B^{(i)}_{\kappa}$ which satisfy

$$e^{\tau\mathcal{D}^{(i)}} = \sum_{\kappa=1}^k B_{\kappa}^{(i)} \otimes \overline{B}_{\kappa}^{(i)}, \quad (17)$$

where k is the *Kraus rank* of the operator $e^{\tau\mathcal{D}^{(i)}}$ [9]. These local acting dissipative time evolution operators can be applied sequentially. The action of one of them on site i is given by

$$e^{\tau\mathcal{D}^{(i)}}(\rho(t)) = \sum_{\kappa=1}^k B_{\kappa}^{(i)} \rho(t) \overline{B}_{\kappa}^{(i)} = \sum_{\kappa=1}^k B_{\kappa}^{(i)} X(t) X^{\dagger}(t) \overline{B}_{\kappa}^{(i)} \quad (18)$$

$$= \sum_{\kappa=1, \kappa'=1}^k \delta_{\kappa, \kappa'} B_{\kappa}^{(i)} X(t) X^{\dagger}(t) \overline{B}_{\kappa'}^{(i)} \quad (19)$$

$$= \sum_{\kappa=1, \kappa'=1}^k B_{\kappa}^{(i)} (X(t) \otimes \langle \kappa |) (X^{\dagger}(t) \otimes | \kappa' \rangle) \overline{B}_{\kappa'}^{(i)} \quad (20)$$

$$= \left(\sum_{\kappa=1}^k B_{\kappa}^{(i)} (X(t) \otimes \langle \kappa |) \right) \left(\sum_{\kappa'=1}^k B_{\kappa'}^{(i)} (X(t) \otimes \langle \kappa' |) \right)^{\dagger}, \quad (21)$$

where $\{|\kappa\rangle\}$ are orthogonal basis vectors. Therefore again we only need to calculate the dissipative time evolution for $X \mapsto \sum_{\kappa=1}^k B_{\kappa}^{(i)} (X(t) \otimes \langle \kappa |)$. In order to perform the whole time evolution for the purified form we use a decomposition of the time evolution operators.

1.4.1 Trotter-Suzuki expansion

The time evolution operator $e^{\tau\mathcal{L}}$ can be approximated by using the second order Trotter-Suzuki expansion, giving

$$e^{\tau\mathcal{L}} = e^{-i\tau H_e/2} e^{-i\tau H_o/2} e^{\tau\mathcal{D}} e^{-i\tau H_o/2} e^{-i\tau H_e/2} + O(\tau^3), \quad (22)$$

meaning the time evolution operator is approximated by this product of operators except for an error scaling with τ^3 [17]. One Trotter-Suzuki expansion approximates the term $e^{\tau(A+B)}$ with $e^{\tau A/2} e^{\tau B} e^{\tau A/2} + O(\tau^3)$. Because the used Hamiltonian can be split into different layers, one associates A with $-i H_e$ and B with $-i H_o + D$ giving $e^{-i\tau H_e/2} e^{\tau(-i H_o + D)} e^{-i\tau H_e/2} + O(\tau^3)$. Accordingly, we treat $e^{\tau(-i H_o + D)}$ in a similar way which gives equation 22.

10

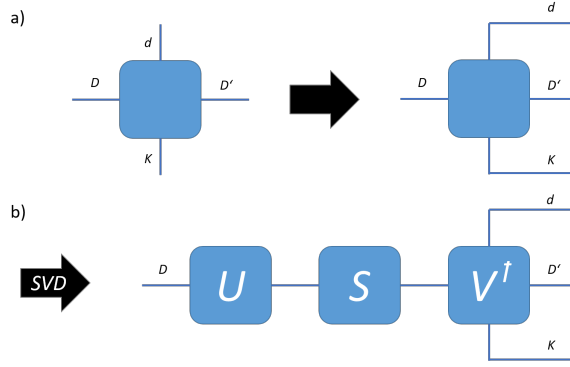


Figure 7: Singular value decomposition (SVD) of one tensor of the MPS in the direction of the right bond dimension. **a)** Merging of the physical dimension j_i to the right bond dimension D . **b)** SVD of the resulting tensor. This gives a diagonal matrix S with the singular values and two matrices U, V^\dagger which are both unitary.

kept depending on the maximal allowed dimension. This process is called *truncation*. The same kind of growth will be in the Kraus dimension due to the contraction of the dissipative operator. However, it has been seen that this discarding of singular values still leads to a reasonable description of the time evolution of the state [9]. All the discarded values are saved, which gives a one norm bound for the time evolution, in the so called *discarded weight* in order to perform an error discussion (see appendix B on page 33) [9]. The positivity of the state would not be guaranteed under time evolution and truncation in the MPO description of a density matrix [18]. But using the time evolution for the purified form of the tensor network this property is conserved in time [9].

The same procedure is done for the odd layers and the second even one. The dissipative layer is applied between the two odd ones. For this the Kraus operators $B^{(i)}$ are applied to the tensor network by contracting them into the local tensor $A^{(i)}$ and merging the Kraus dimension K between the tensor and its adjoint counterpart $\bar{A}^{(i)}$ with the connection of the Kraus operators k_i (see figure 9) [11]. This increases the Kraus dimension, so a SVD is performed to reduce it (see figure 9c). After that process the products of the SVD are contracted to one tensor again.

1.4.3 Calculating expectation values

Tensor networks exhibit gauge invariants [12], meaning many tensor networks are possible for an identical representation of one physical state. This can be seen from the fact that it is possible to insert identities $\mathbb{1} = SS^{-1}$ between two tensors of the network without changing the whole state. This allows for example to insert pairs of unitary matrices to change local

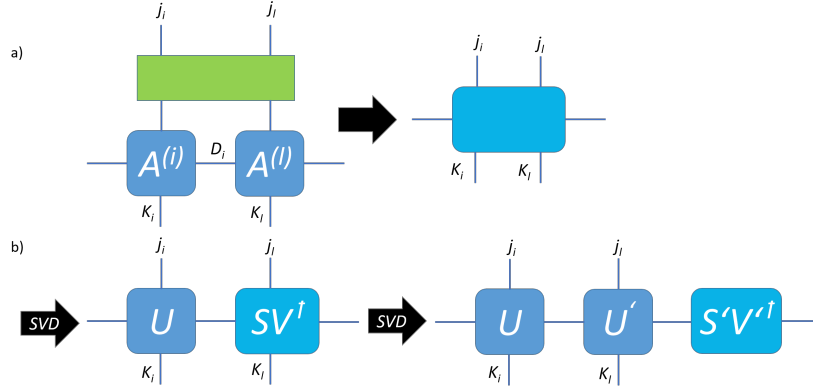


Figure 8: Applying the even time evolution layer on the neighbouring sites i and $l = i + 1$. **a)** Contraction of the physical and the bond dimension between the tensors $A^{(i)}$ and $A^{(l)}$ and the time evolution operator of the even layer $e^{-i\tau H_{e,i}}$. **b)** The resulting tensor of the two sites is split by a SVD. Then a second SVD is performed and the part $S'V'^\dagger$ is contracted in the next tensor, leaving two unitary tensors U and U' on the sites i and l .

tensors. A particularly important gauge fixation is the so called *mixed normalised form*. In the mixed normalised form for a chosen site $i \in \{1, \dots, N\}$ all sites $l < i$ are left normalised, meaning they fulfil

$$\sum_{\alpha; j_l} \bar{A}_{\alpha, \beta; j_l}^{(l)} A_{\alpha, \gamma; j_l}^{(l)} = \delta_{\beta, \gamma}, \quad (23)$$

whereby j_l denotes the index of the combined physical and Kraus dimension and α, β, γ are the indices of the bond dimensions [12] (see figure 10a). Therefore this contraction leaves us with an identity. In addition the sites $r > i$ are right normalised, meaning they fulfil

$$\sum_{\alpha; j_r} A_{\alpha, \beta; j_r}^{(r)} \bar{A}_{\alpha, \gamma; j_r}^{(r)} = \delta_{\beta, \gamma}, \quad (24)$$

with the same notation as above (see figure 10b). Practically we are normalising the whole tensor network for instance to the left border, meaning that SVDs are performed in the direction of the bond dimension starting from the right border. In each step (see figure 7) we contract the products S and V^\dagger of the SVD to the tensor on the left and then the same thing is repeated with that tensor. As a result we get a unitary tensor $U^{(i)}$ on each site, beside the first one (right normalised form for the first site). We are now able to compute the expectation value of any observable which is only acting on the first site by contracting the whole tensor network. This can be done very efficiently, because all the contractions besides on the first site compute to the identity. For the expectation value of the second site we simply move the normalisation there, by performing an SVD of the first site to the

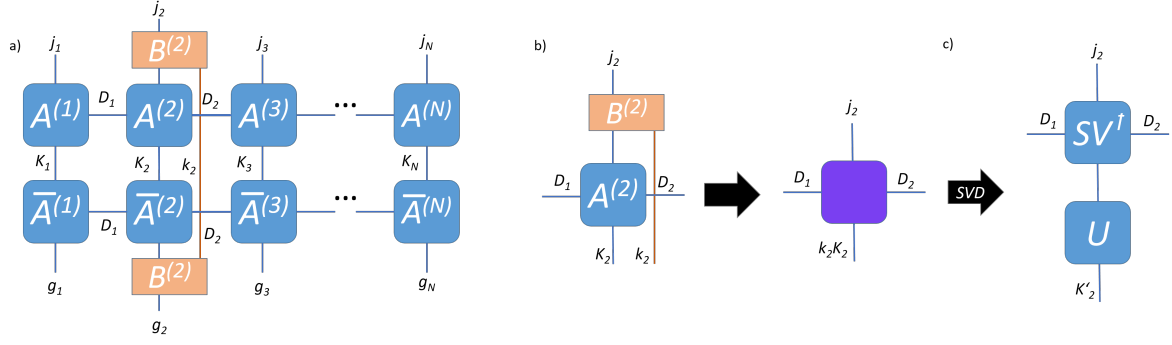


Figure 9: Applying the dissipative layer for site two. **a)** Applying the local Kraus operators of site two $B^{(2)} = \sum_{\kappa} B_{\kappa}^{(2)} \otimes \langle \kappa |$ to the tensor network (see equation 18). The connection k_2 between them is merged to the Kraus dimension K_2 between the tensors of site two. **b)** Contracting the dissipation operator $B^{(2)}$ into the tensor $A^{(2)}$. This leads to a tensor with a bigger Kraus dimension $k_2 \cdot K_2$. **c)** A SVD is performed to reduce the Kraus dimension to the given threshold. Afterwards the products are contracted back together.

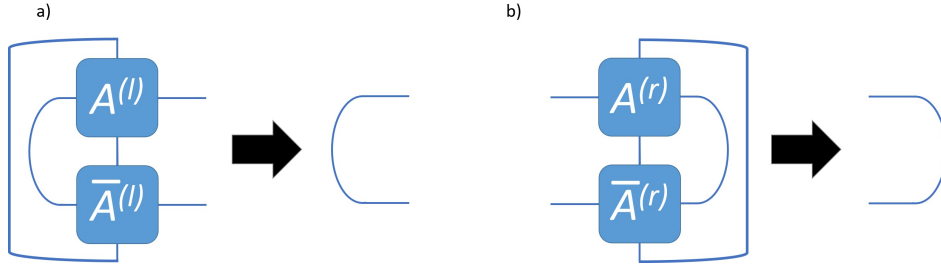


Figure 10: Normalisation process for a tensor network. The two corresponding tensor are contracted together which leaves the identity. The physical and the Kraus dimension are merged and contracted together and the corresponding bond dimension is contracted as well. **a)** One tensor pair of the left normalised form. **b)** One tensor pair of the right normalised form.

other direction, leaving on the first site the unitary tensor $U^{(1)}$. Therefore we have the mixed normalised form for the second site now. This can be done sequentially for all other sites. So the computational cost of this is scaling linear with the system size N .

2 Many-body localisation

The investigation of transport in quantum many-body systems is one of the most active fields in condensed matter physics. Realistic systems are not perfect, because they have e.g. impurities. Therefore particles in a given real system do not see a translation invariant lattice, but a lattice with defects. Therefore the impact of this kind of disorder on transport is a key question and if this leads to a breakdown of transport, due to the interference of non classical waves.

2.1 Anderson localisation

Anderson was the first to study theoretical disordered systems in 1958 [2]. He investigated theoretically non interacting electrons on an infinite lattice. In one dimension the corresponding Hamiltonian reads

$$H = -J \sum_i (f_i^\dagger f_{i+1} + f_{i+1}^\dagger f_i) + \sum_i \Delta_i f_i^\dagger f_i, \quad (25)$$

whereby f_i^\dagger is the creation operator for fermions on site i (and f_i the annihilation one).

Hopping The first term captures the discrete kinetic energies of the particles in the lattice, i.e. the lattice laplacian, which describes *hopping* between neighbouring sites (tight-binding model) with the hopping strength J . So a particle on site i will spread over the whole lattice under time evolution, due to the possible tunnelling to neighbouring sites.

Disorder potential The second sum describes the random disorder potentials with the random factor Δ_i drawn from some interval, whereby the range of the interval equals to the disorder strength. This represents a random factor from, for example, the surrounding material like a discontinuity or impurities. In this case we have frozen disorder, meaning that the hopping happens much faster than any changes to the disorder potentials. Therefore we assume the disorder potentials as constant in time.

This Hamiltonian does not support any interactions between the electrons. Anderson found that this system shows localisation even for small disorder strengths, meaning there are only localised wave functions of the electrons which are decaying exponentially in the distance. As a result any transport (particle and correlation) in the lattice is shut down, preventing the system from reaching thermal equilibrium, thus making it an isolator. This is called *Anderson localisation* [5].

2.2 Many-body localisation

The next question is, how stable this localisation effects are under the interaction between particles. Let us now look at one-dimensional systems with interactions between neighbouring particles, with the Hamiltonian

$$H = -J \sum_i (f_i^\dagger f_{i+1} + f_{i+1}^\dagger f_i) + \sum_i \Delta_i f_i^\dagger f_i + U \sum_i n_i n_{i+1}, \quad (26)$$

whereby $n_i = f_i^\dagger f_i$ is the particle number operator.

Interaction between neighbouring sites The third term describes the interaction between particles on neighbouring sites with the interaction strength U . This models for example the repulsive Coulomb force of charged spinless particles.

One can observe to some extent a similar behaviour to the Anderson localisation. Disorder can also cause a break down in the particle transport, preventing thermalisation. But this depends on the disorder strength and the energy of the system: For small disorder strengths there can be particle transport if the energy is high enough and for high enough disorder strengths the transport breaks down for every energy [5]. In contrast to the Anderson localisation the correlation increases unbounded slowly in time in any case, because of the interaction [7]. The intuition behind this growth is that the time evolution of a product state under a Hamiltonian with disorder leads first to a spread of the correlation in the lattice linearly in time, but at a certain point, depending on the disorder strength, this growth of the correlation will be slowed down to a logarithmically leaking out of a localisation region. This behaviour can be understood by the existence of local constants of motion and could be captured rigorously by Lieb-Robinson bounds [8]. Moreover, this allows the transport of information. It is not clear at the moment if such a behaviour could not still lead to a thermalisation of the system, because of some small particle transport for very long time scales, making the state not a stable state of the system, but a meta stable state [6]. However, assuming localisation for all time scales some information of the initial state is retained. It is still being discussed when one should speak of many-body localisation and how it could be assessed in experiments. Therefore a lot of experiments and theoretical studies investigate this topic and two example experiments will be discussed in the next section.

2.3 Experimental observation of many-body localisation

A recent experiment of the group of I. Bloch at the Max Planck Institute of quantum optics in Munich investigated the behaviour of cold fermions in a one-dimensional optical lattice to

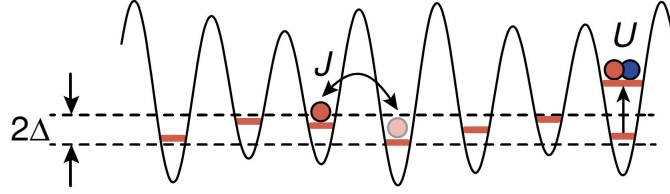


Figure 11: Visualisation of a system on which a Hamiltonian acts. The Hamiltonian supports hopping between neighbouring sites (J), random disorder (Δ_i), which changes the energy levels of the sites (brown bars), and on-site interaction between particles on the same site (U), which also alters the energy level. *Source:* [3]

analyse many-body effects [3]. They initialise the state by producing a charged density wave, with a ^{40}K atom on every second site, which behave like fermions with a spin. Due to the Pauli-principle there can be maximal two fermions with different spins on each site. To start the experiment they lowered the potential of the optical lattice to allow hopping between the sites. The main observable was the *imbalance* I which is derived from the number of fermions on even sites N_e and on odd sites N_o with

$$I = \frac{N_e - N_o}{N_e + N_o}. \quad (27)$$

The imbalance is a good indicator for localisation effects: The imbalance of the initial state is one and without any disorder the system thermalises, thus having an imbalance of zero. If the system fails to thermalise due to disorder, there are more particles on even sites than on odd ones, because they are localised there. In this case the imbalance does not reach zero. The dynamic of the system is given by the Hamiltonian

$$H = -J \sum_{i,\sigma} (f_{i,\sigma}^\dagger f_{i+1,\sigma} + f_{i+1,\sigma}^\dagger f_{i,\sigma}) + \Delta \sum_{i,\sigma} \cos(2\pi\beta i + \phi) f_{i,\sigma}^\dagger f_{i,\sigma} + U \sum_i n_{i,\uparrow} n_{i,\downarrow}, \quad (28)$$

whereby we use the same notation as before with now $\sigma \in (\uparrow, \downarrow)$ for spins. The overall disorder strength Δ can be adjusted in the experiment. Furthermore, β is chosen to incommensurate to the periodicity of the lattice in order to create a pseudo random potential for the lattice with an offset ϕ . A visual representation of the Hamiltonian can be seen in figure 11.

They observed many-body localisations effects in the case of disorder in their experiments. So some particles on the even sites were trapped and therefore the initial state to some extent retained (see figure 12). This was done for different combinations of the parameters J , Δ and U . They could clearly see a stronger localisation effect (a higher imbalance saturation value) for stronger disorder potentials (see figure 12). A comparison between their results and my

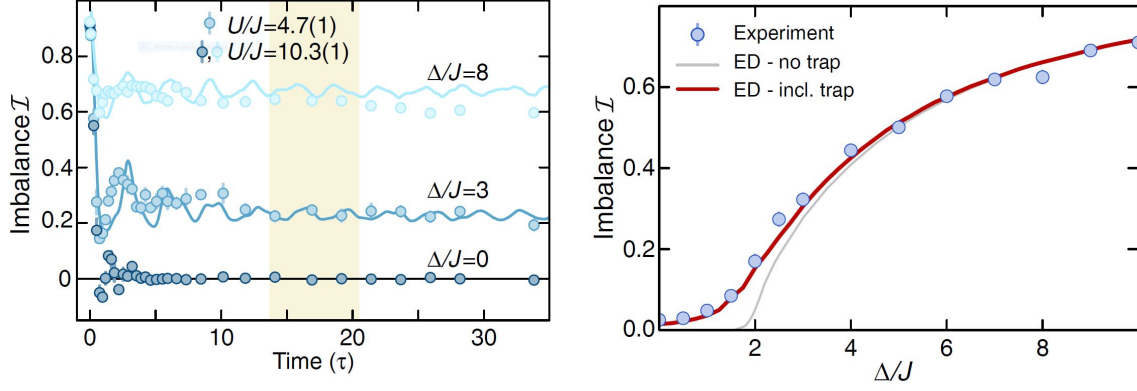


Figure 12: Left Time evolution of a fermion chain for different disorder realisations. The Hamiltonian is described in equation 28 and a visual representation can be seen in figure 11. The expected localisation effects under disorder can be seen. The dots with the error bars represent their actual measurements and the lines are their theoretical expectations. *Source:* [3]. **Right** Saturation values of the imbalance I for different disorder realisations. These are computed from simulations similar to the one in the left picture. The dots are the experimental values and the lines the theoretical ones. *Source:* [3]

simulations can be found in 3.2.3 on page 21.

The system in this experiment is nearly completely decoupled from the surroundings, so the influence of the surroundings was not investigated. But as mentioned, all real systems interact with their environment, therefore another experiment with a similar set up was performed in the group of I. Bloch at the Max Planck Institute of quantum optics [4]. They investigated now the behaviour of localised quantum many-body systems under the influence of photons which are scattered on the fermions and lead to particle loss to the environment. They observed an exponential decay of the initial density pattern with a rate that depends linearly on the scattering rate [4]. For a comparison with our simulations see appendix C on page 36. Therefore, it is interesting to look at systems which show localisation due to disorder and interact with their environments.

3 Simulation and results

In this section we present the results of our tensor network simulations. The program used for these simulations is written in python 2.7 and is based on the algorithm presented in [9], which is partly discussed in 1.4. The code can be obtained from the attached CD.

3.1 Realisations

We consider similar systems to the one in the experiment in section 2.3 to investigate the existence of many-body localisation effects in these systems depending on interaction, dissipation and disorder. The main observable we consider is the imbalance I (see equation 27) of the evolved states. The imbalance I can be calculated by computing the expectation value (see 1.4.3 on page 11) of the local particle number operator for each site. All simulated systems start in an initial state with maximal imbalance $I = 1$. This means that all even sites are maximally occupied and all odd sites empty. For instance, in the case of spinless fermions we have

$$|\psi_0\rangle = |1, 0, 1, 0, \dots, 1, 0\rangle. \quad (29)$$

Then the time evolution of the system is observed based on the imbalance. This is exhibited for four different systems with different interactions to the environment:

- **Isolated spinless fermionic chain** A fermionic chain isolated from the environment, with twice as many sites as fermions and only one fermion per site is allowed. So there is no influence from the environment and the fermion number is conserved.
- **Spinless fermionic chain with local dephasing** The system is the same as the above, but now coupling with the environment is allowed with local dephasing.
- **Spinless fermionic chain with particle loss** Again similar to the above system, but the interaction with the environment is now only particle loss to an external bath.
- **Spinful fermionic chain with on-site interaction and local dephasing** The system used in the experiment is modelled (see 2.3 on page 15): The fermions now have a spin degree of freedom and therefore two fermions are allowed per site. The initial state has two fermions (singlet) on each second site. Moreover, we study the effect of local dephasing.

In each of the systems there are three parameters which can be modified: Hopping strength J , disorder strength Δ and interaction strength U which are described in section 2 on page 14. Moreover, for the dissipative systems the coupling strength with the environment γ , which is described later in 3.2.2 on page 21, can also be modified. We study the interplay between these parameters for the different systems and the resulting imbalance equilibria to see how they influence the localisation effects. In addition, we fixed the hopping strength J to one, in order to describe the other parameters in relation to it. The following ranges for the parameters were used:

- Hopping strength: $J = 1$
- Disorder strength: $\Delta \in [0, 20]$
- Interaction strength $U \in [0.5, 2]$
- Coupling strength to the environment $\gamma \in [0, 10]$

For each different combination of parameters which include a non zero disorder strength, 20 simulations are performed. This is done in order to average over the imbalance values for the different random disorder values. An example plot for the time evolution of the different disorder realisations can be seen in appendix A on page 33.

3.2 Spinless fermionic chain

At first we look at spinless fermions with an interaction between neighbouring sites. Furthermore, only one particle per lattice site is allowed. Although the main focus in this thesis lies on localisation effects under dissipation, it is also interesting to study many-body localisation in isolated systems like in the described experiment. Therefore, simulations were done with and without different kinds of dissipation.

3.2.1 Setting

The Hamiltonian of this system without disorder reads

$$H = -J \sum_{i=1}^N (f_i^\dagger f_{i+1} + f_{i+1}^\dagger f_i) + U \sum_{i=1}^N n_i n_{i+1}, \quad (30)$$

with the usual notation. To fit this Hamiltonian with the program which is for spin-states we need to describe the fermionic operators with spin operators. This means we are performing

a transformation from $|0\rangle$ for no fermion and $|1\rangle$ for one fermion on a site as the basis to spin-up $\begin{pmatrix} 1 \\ 0 \end{pmatrix}$ and spin-down $\begin{pmatrix} 0 \\ 1 \end{pmatrix}$. This can be done in one dimension with the Jordan-Wigner transformation [19]. We find corresponding expressions for the creation and annihilation operators:

$$S^- = \frac{1}{2}(\sigma_x - i\sigma_y) = \begin{pmatrix} 0 & 0 \\ 1 & 0 \end{pmatrix} \quad (31)$$

$$S^+ = \frac{1}{2}(\sigma_x + i\sigma_y) = \begin{pmatrix} 0 & 1 \\ 0 & 0 \end{pmatrix} \quad (32)$$

Unfortunately, these are not the direct equivalents to the fermionic ones, but they have the connection [19]

$$f_i^\dagger = \left(\prod_{j=1}^{i-1} \sigma_{zj}\right) S_i^- \quad (33)$$

$$f_i = \left(\prod_{j=1}^{i-1} \sigma_{zj}\right) S_i^+. \quad (34)$$

These expressions do not act locally on a single site only and all the advantages with it would be lost. So it is not possible to use a single fermionic operator, but in nearest neighbour products of the creation and annihilation operator these factors disappear due to

$$f_i^\dagger f_{i+1} = \left(\prod_{j=1}^{i-1} \sigma_{zj}^2\right) S_i^- \sigma_{zi} S_{i+1}^+ = S_i^- S_{i+1}^+ \quad (35)$$

$$f_{i+1}^\dagger f_i = \left(\prod_{j=1}^{i-1} \sigma_{zj}^2\right) \sigma_{zi} S_i^+ S_{i+1}^- = S_{i+1}^- S_i^+, \quad (36)$$

because $\sigma_z^2 = \mathbb{1}$; $S_i^+ \sigma_{zi} = S_i^+$ and $\sigma_{zi} S_i^- = S_i^-$. Accordingly, the particle number operator n can be written in the spin picture as

$$n = f_i^\dagger f_i = S^- S^+ = \frac{1}{2}(\mathbb{1} - \sigma_z) = \begin{pmatrix} 0 & 0 \\ 0 & 1 \end{pmatrix}. \quad (37)$$

Therefore, the resulting Hamiltonian in the spin picture is

$$H = -J \sum_{i=1}^N (S_i^- S_{i+1}^+ + S_{i+1}^- S_i^+) + \sum_{i=1}^N n_i n_{i+1}. \quad (38)$$

The disorder term we use is quite similar to the one in the experiment. Instead of the particle number operator n we use only σ_z which is not a big difference as seen in equation 37. The only difference the additional $\mathbb{1}$ makes is a constant shift of the energy which does not have

any impact. Moreover, instead of the term $\cos 2\pi\beta i + \phi$, we use random factors $\Delta'_i \in [-1, 1]$. Additionally, the disorder term does not act on the last site. Therefore, the full Hamiltonian reads

$$H = -J \sum_{i=1}^N (S_i^- S_{i+1}^+ + S_{i+1}^- S_i^+) + \Delta \sum_{i=1}^N \Delta'_i \sigma_{zi} \mathbb{1}_{i+1} + U \sum_{i=1}^N n_i n_{i+1}. \quad (39)$$

3.2.2 Dissipation

As discussed in 1.4 on page 7 all real quantum systems interact to some extent with their environment. First we are looking at dephasing, an interaction which acts like a measurement. To capture this in terms of Lindblad-operators $L^{(i)}$ we set

$$L_1^{(i)} = \frac{1}{2} \sqrt{\gamma} (\mathbb{1} - \sigma_z)_i \quad (40)$$

$$L_2^{(i)} = \frac{1}{2} \sqrt{\gamma} (\mathbb{1} + \sigma_z)_i, \quad (41)$$

because this projects the local states to $|1\rangle$ or $|0\rangle$ which is basically the same effect as a measurement. The strength of the projection is controlled by the coupling parameter γ which is multiplied to $L_1^{(i)}$ and $L_2^{(i)}$ as a square root. A larger coupling strength γ corresponds to a more frequent measurement from outside. Therefore, without any dissipation a system is simulated which is isolated from its environment.

3.2.3 Results of the spinless isolated fermionic chain

The size of the chain is $N = 32$ and it is occupied by 16 fermions. Because we do not have any interaction with the environment, the dissipative layer is not applied in this simulation. This leads to a slightly different Trotter-Suzuki expansion without a dissipative layer [17]. Therefore, the two odd layers can be applied together and we have only a total of three layers. We set the Kraus dimension to one and the limit for the bond dimension to 300. A total of 400 time steps of $\tau = 0.01$ is performed for each simulation. The resulting time evolution can be seen in figure 13 for disorder strengths $\Delta \in [0, 20]$ and an interaction strength of $U = 1$. The expected trend for the graphs is clearly visible: For the realisation without disorder the imbalance value oscillates around zero and the amplitude decreases with time. For the disorder realisations the equilibrium is not reached, but the imbalance also oscillates around a saturation value ($I \neq 0$). These results are in good agreement with the experiment (see 2.3 on page 15). For larger disorder strengths Δ the imbalance value I also increases. In order to compare these realisations better, the value for the saturation is taken as the mean of the imbalance values after the time $T = 2.0$. This is justified, because the imbalance

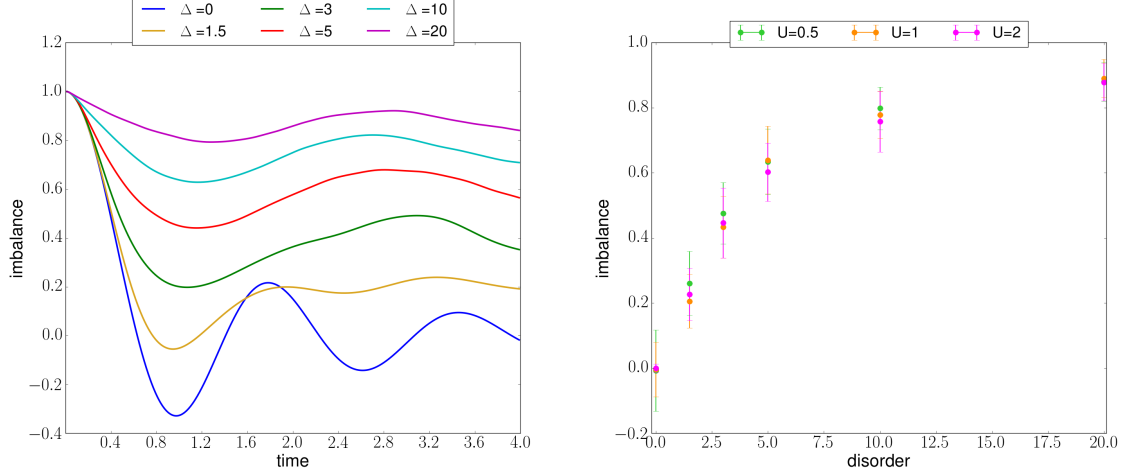


Figure 13: Time evolution for the isolated spinless fermionic chain with $N = 32$ sites. The Hamiltonian is described in equation 39. For each non zero disorder strength Δ we show the averaged imbalance values over 20 different disorder realisations. A similar behaviour to the discussed experiment can be seen (see 2.3 on page 15). **Left** Time dependence of the imbalance I is shown for different disorder realisations with fixed interaction strength $U = 1$. The expected memory effects are clearly visible. The saturation value of the imbalance grows with the disorder strength. **Right** The saturation values are taken as the mean of the imbalance values after the time $T = 2.0$. The growth of the imbalance saturation value for higher disorder realisations can be seen for different interaction strengths U . Due to large errors compared to the differences between the saturation values for different interaction strengths, we can not conclude on a dependence. The errors emerge from the averaging processes (see appendix B on page 33).

does not change too much any more at this point or oscillates around a saturation value. This holds also true for the other combinations of the parameters. For the computation of the errors for the saturation values see appendix B on page 33. Therefore, the imbalance saturations can be plotted against the disorder strength for different values of the interaction strength U (see figure 13). The trend of the imbalance saturation is compatible with the ones in the experiment (see figure 12): For small disorder values the corresponding imbalance saturation increases drastically, but this increase is slowed down for larger disorder values. Furthermore, the saturation values for different interaction strengths do not differ enough to enable conclusions about this influence, because the errors are too large.

3.2.4 Results of the spinless fermionic chain with dephasing

Now we turn on the coupling with the environment, but leave the rest of the setting unchanged. Since we now have to take into account open system dynamics the run time increases

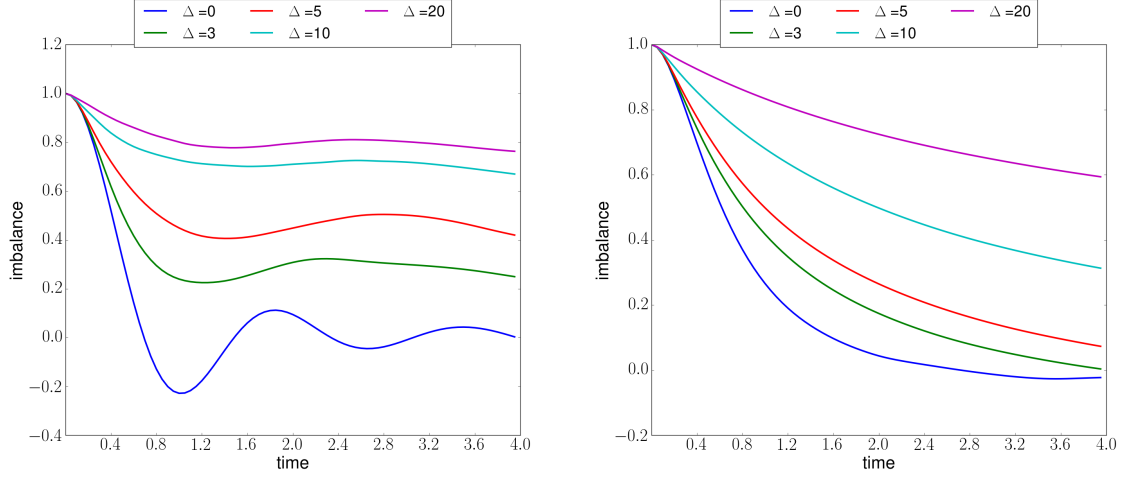


Figure 14: Time evolution for the spinless fermionic chain with $N = 16$ sites and with dephasing. The Hamiltonian is described in equation 39 and the used Lindblad-operators are shown in equation 40. For each non zero disorder strength, we perform 20 simulations for different disorder realisations and compute the averaged imbalance. **Left** The time dependence of the imbalance I is shown for different disorder realisations. The interaction strength is set to $U = 1$ and the coupling with the environment to $\gamma = 0.5$. Despite the dissipation we still see localisation for this time scale. **Right** The coupling strength is $\gamma = 5$. In this case the expected loss of localisation is clearly visible. The imbalance value I decreases exponentially and oscillations are suppressed.

dramatically, therefore a smaller system is used, in order to get results with an acceptable discarded weight in reasonable time for this Bachelor's Thesis (for the error discussion see appendix B on page 33). The system size is chosen to be $N = 16$. The limit for the Kraus dimension is set to 30 and for the bond dimension to 30 as well. A total of 80 time steps of $\tau = 0.05$ is performed for each simulation, which gives the same total time as before.

The dissipation will lead to thermalisation for any disorder realisation, due to the loss of coherence, but it might take quite some time depending on the disorder and coupling strength [4]. This means that for small coupling strengths $\gamma \leq 1$ we still see localisation for our investigated time scales (for an example see figure 14). Therefore, we can compute and compare saturation values for these, whereby the calculation process is the same as in the previous section. We compare the saturation values of different low coupling values γ for the different disorder strengths Δ and for a constant interaction strength $U = 1$ (see figure 15). The dependence of the imbalance saturation value on the disorder is similar to the one without dissipation (see figure 13). Moreover, in this case also the influence of the dephasing is clearly visible: For a higher coupling strength, but the same disorder, we get a lower saturation value, which is as expected.

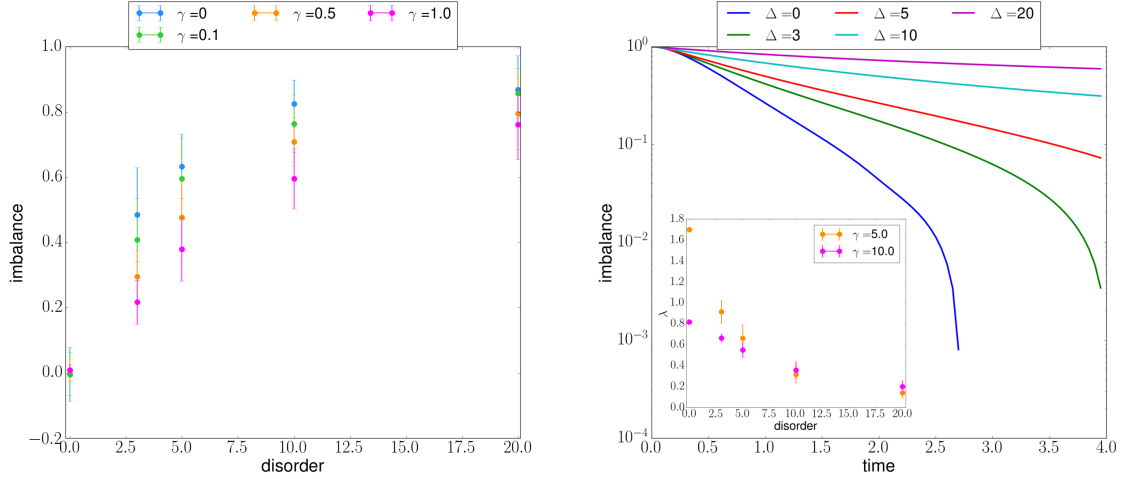


Figure 15: Influence of the coupling strength γ to the imbalance value I . The time evolution is done for the spinless fermionic chain with $N = 16$ sites and with dephasing. **Left** For low coupling strengths ($\gamma \leq 1$) the saturation values for the imbalance I of simulations as seen in figure 14 were taken and plotted against the disorder strength. The saturation values increase for higher disorder realisations as in the isolated case (see figure 13). Furthermore, the expected influence of the dephasing is clearly visible: The saturation value is lower for a higher coupling parameter γ , whereby all other parameters stay the same. **Right** In contrast to that we do not have localisation for higher coupling strengths ($\gamma > 1$), because we have an exponential decay of the imbalance value I . This is clearly visible in the logarithmic plot. When the imbalance value reaches zero, also negative values are encountered and we do not see the exponential decay any more. In the insert we show a comparison for the dependence of the decay constant λ from the disorder Δ for different coupling strengths γ . In the case of small disorder strengths, it is interesting to see, that the decay constant λ is larger for small coupling strengths than for large ones.

For higher coupling strengths $\gamma > 1$ the imbalance values decrease exponentially over time, all oscillations are suppressed and we do not reach any saturation value besides zero (see figure 14 and figure 15). Accordingly, we can not calculate a saturation value, but in order to compare different coupling strengths γ we compare the decay constants λ (see insert in figure 15). The decay constant λ is defined by fitting a line for the exponentially decaying part by using linear regression for each different disorder realisation. After that the mean value is taken and we use the standard deviation as an error, because the errors of the linear regression are very small. However, in the cases without disorder we use the error from the linear regression. An interesting observation here is that the decay rate for low disorder strengths is higher for a smaller coupling strength. Furthermore, this difference vanishes for higher disorder strengths. An explanation for this is that both disorder and dephasing suppress particle transport. Therefore, for small disorder strengths only the coupling strength

is important for the particle transport and accordingly the thermalisation process is faster for the low coupling strength. Therefore, for high disorder strengths the influence of the coupling strength is less important, because the transport is already suppressed by the disorder.

Moreover, it can still be seen that a higher disorder value Δ leads to a slower thermalisation process. The influence of the coupling strength γ is similar to the one for small coupling strengths, meaning a higher value of γ leads to a lower imbalance value I . In this case this corresponds also to a faster thermalisation process. Overall the expected effects of dephasing to localised systems could be shown: For small coupling parameters we still get localisation effects for our time scales and for higher ones all systems thermalise, whereby the coupling strength and the disorder strength influence the time scales.

3.2.5 Spinless fermionic chain with particle loss

Until now we looked at a conserved number of particles, but a real system could also lose particles to the environment (see [4]). For that we assume that the only interaction with the environment is the particle loss. To this end we need a slightly different set-up: Instead of one fermionic chain we now also use a second one with a trivial dynamic which particles from the original chain can jump to. Each site of the original chain has one corresponding site in the second chain. This means that we can describe this with a four dimensional basis (meaning four physical dimensions) combining every two corresponding sites to one:

$$|0, 0\rangle \Leftrightarrow \text{no fermion}$$

$$|0, 1\rangle \Leftrightarrow \text{fermion on the second chain}$$

$$|1, 0\rangle \Leftrightarrow \text{fermion on the original chain}$$

$$|1, 1\rangle \Leftrightarrow \text{fermions on both chains}$$

The Hamiltonian only acts on the original chain and therefore all operators on the second one are the identity $\mathbb{1}$. That gives us the new operators

$$\tilde{S}^{\pm} = S^{\pm} \otimes \mathbb{1} \quad (42)$$

$$\tilde{\sigma}_z = \sigma_z \otimes \mathbb{1} \quad (43)$$

$$\tilde{n} = n \otimes \mathbb{1}. \quad (44)$$

Accordingly, the new Hamiltonian is given by

$$H = -J \sum_{i=1}^N (\tilde{S}_i^+ \tilde{S}_{i+1}^- + \tilde{S}_{i+1}^+ \tilde{S}_i^-) + \Delta \sum_{i=1}^N \Delta'_i \tilde{\sigma}_{zi} \mathbb{1}_{i+1} + U \sum_{i=1}^N \tilde{n}_i \tilde{n}_{i+1}. \quad (45)$$

The second chain is needed in order to conserve the locality of the model, because a single annihilation operator f^\dagger acting on the first chain would become non local under the Jordan-Wigner transformation [19]. Therefore also a creation operator which acts on the second chain is necessary to recover locality. Accordingly, the Lindblad-operators $L^{(i)}$ have to be different to the previous system, as they are now supposed to transfer a particle from the one chain to the other. So they read

$$L^{(i)} = \sqrt{\gamma} \cdot \tilde{S}^+(\sigma_z \otimes S^-) = \sqrt{\gamma} \begin{pmatrix} 0 & 0 & 0 & 0 \\ 0 & 0 & -1 & 0 \\ 0 & 0 & 0 & 0 \\ 0 & 0 & 0 & 0 \end{pmatrix}. \quad (46)$$

All this simulates the same lattice with the same Hamiltonian as before, but now with particle loss instead of the dephasing.

For the simulations with particle loss the size of the chain is again set to $N = 16$. The limit for the Kraus dimension is set to 10 and for the bond dimension to 50. The sufficiency of the smaller Kraus dimension is discussed in appendix B on page 33. As previous 80 time steps of $\tau = 0.05$ are taken for each simulation. For high dissipation values $\gamma > 1$ the particle number decreases very fast, which results in a nearly empty first chain. Even though we still obtain values for the imbalance, at this point the dynamic of the system is not well described by the simulations, because the particle number decays too fast. In this case the system is not of experimental interest, as the system is clearly unstable for very high coupling strengths. However, it is still interesting to study this decay process and compare it to the results of the experiment, where low coupling strengths were investigated (see 2.3 on page 15). We found that the decay rate is proportional to the coupling strength (see appendix C on page 36), which is also the observation of the experiment [4].

For low coupling values $\gamma \leq 1$ we can make a similar analysis as before. The time evolution is shown in figure 16 for a coupling strength $\gamma = 0.5$ and interaction strength $U = 1$. Again the localisation effects are clearly visible and saturation values can be computed. These are shown for different coupling strengths also in figure 16. The overall time evolution is very close to the one with dephasing. However, in the case of particle loss the influence of the coupling strength on the saturation value is much smaller than the influence in the case of dephasing (see figure 15), because due to the error bounds we cannot separate the individual points for a given disorder strength.

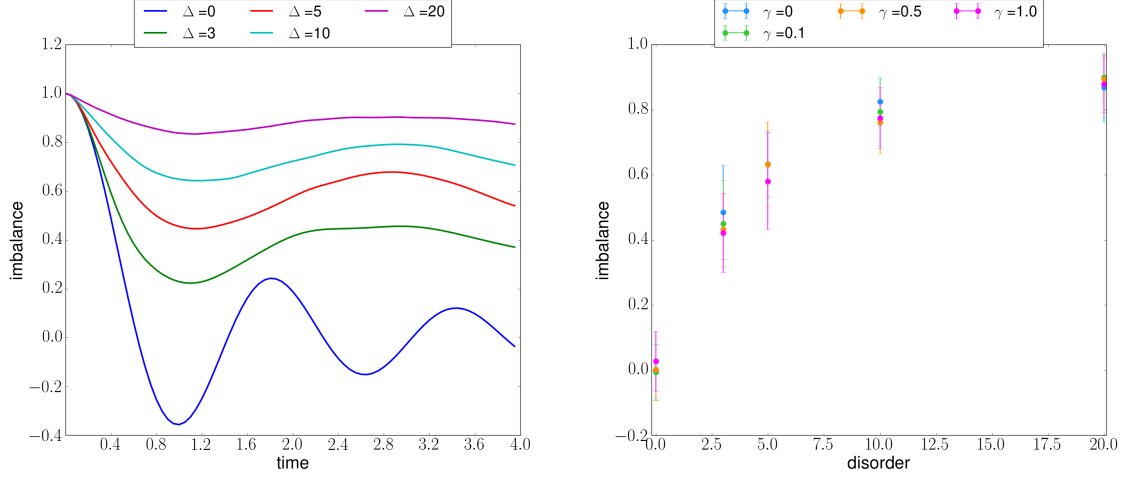


Figure 16: Time evolution and imbalance saturation values for the spinless fermionic chain with $N = 16$ sites and with particle loss with low coupling strengths ($\gamma \leq 1$). The Hamiltonian is described in equation 45 on page 25 and the Lindblad-operator in equation 46. **Left** The time dependence of the imbalance I is shown for different disorder realisations with fixed interaction strength $U = 1$ and fixed coupling strength $\gamma = 0.5$. As previously described we show averaged imbalance values with respect to 20 disorder realisations for each non zero disorder strength Δ . The expected memory effects are again clearly visible. **Right** The saturation values of the imbalance are plotted against the disorder strength. For the computation of the errors see appendix B on page 33. The dependence on the disorder is similar to the results for the chain with dephasing instead of particle loss (see figure 15), but the influence of the different coupling strengths is not visible.

3.3 Spinful fermionic chain

The previously investigated systems were simplified in order to allow different kinds of dissipation and to be able to perform simulation for bigger systems. This was achieved by allowing only one particle per site and having an interaction between neighbouring sites. To study if these previous simplifications of the Hamiltonian nevertheless approximate the Hamiltonian of the experiment (equation 28), we now investigate this Hamiltonian. This system allows two fermions on a single site with different spin states. Therefore, we can have four different states on each site:

$$|0, 0\rangle \Leftrightarrow \text{no fermion}$$

$$|0, 1\rangle \Leftrightarrow \text{fermion with spin-up}$$

$$|1, 0\rangle \Leftrightarrow \text{fermion with spin-down}$$

$$|1, 1\rangle \Leftrightarrow \text{two fermion singlet}$$

To get the spin-operators for this system we can again perform a Jordan-Wigner transformation [19]. This time we get the connection

$$f_{i,\sigma}^\dagger = \left(\prod_{j=1}^{i-1} Z_j \right) S_{i,\sigma}^- \quad (47)$$

$$f_{i,\sigma} = \left(\prod_{j=1}^{i-1} Z_j \right) S_{i,\sigma}^+, \quad (48)$$

with $\sigma = \uparrow, \downarrow$ and

$$Z = \sigma_z \otimes \sigma_z = \begin{pmatrix} 1 & 0 & 0 & 0 \\ 0 & -1 & 0 & 0 \\ 0 & 0 & -1 & 0 \\ 0 & 0 & 0 & 1 \end{pmatrix}; S_\uparrow^+ = \begin{pmatrix} 0 & 1 & 0 & 0 \\ 0 & 0 & 0 & 0 \\ 0 & 0 & 0 & 1 \\ 0 & 0 & 0 & 0 \end{pmatrix}; S_\downarrow^+ = \begin{pmatrix} 0 & 0 & 1 & 0 \\ 0 & 0 & 0 & -1 \\ 0 & 0 & 0 & 0 \\ 0 & 0 & 0 & 0 \end{pmatrix},$$

whereby the creation operators are transposed annihilation operators $S_\uparrow^- = S_\uparrow^{+T}$ and $S_\downarrow^- = S_\downarrow^{+T}$. Again is $Z^2 = \mathbb{1}$ and therefore $N_\sigma = f_\sigma^\dagger f_\sigma = S_\sigma^- S_\sigma^+$. But in contrast to the Jordan-Wigner transformation for $d = 2$ this time we have $S_{i,\sigma}^- Z_i \neq S_{i,\sigma}^-$ and $Z_i S_{i,\sigma}^+ \neq S_{i,\sigma}^+$. Accordingly, the product of creation and annihilation operators differs from equation 35 as

$$f_{i,\sigma}^\dagger f_{i+1,\sigma} = \left(\prod_{j=1}^{i-1} Z_j^2 \right) S_{i,\sigma}^- Z_i S_{i+1,\sigma}^+ = \tilde{S}_{i,\sigma}^- S_{i+1,\sigma}^+ \quad (49)$$

$$f_{i+1,\sigma}^\dagger f_{i,\sigma} = \left(\prod_{j=1}^{i-1} Z_j^2 \right) Z_i S_{i,\sigma}^+ S_{i+1,\sigma}^- = S_{i+1,\sigma}^- \tilde{S}_{i,\sigma}^+, \quad (50)$$

with $\tilde{S}_{i,\sigma}^- = S_{i,\sigma}^- Z_i$ and $\tilde{S}_{i,\sigma}^+ = Z_i S_{i,\sigma}^+$. As a result, the equivalent Hamiltonian to equation 28 adds up to

$$H = -J \sum_{i=1}^N \sum_{\sigma=\uparrow,\downarrow} (\tilde{S}_{i,\sigma}^- S_{i+1,\sigma}^+ + S_{i+1,\sigma}^- \tilde{S}_{i,\sigma}^+) + \Delta \sum_{i=1}^N \sum_{\sigma=\uparrow,\downarrow} \Delta'_i N_{i,\sigma} + U \sum_{i=1}^N N_{i,\uparrow} N_{i,\downarrow}. \quad (51)$$

The four Lindblad-operators are again the projectors to the basis (similar to equation 40) and the particle number operator n has the form

$$n = \begin{pmatrix} 0 & 0 & 0 & 0 \\ 0 & 1 & 0 & 0 \\ 0 & 0 & 1 & 0 \\ 0 & 0 & 0 & 2 \end{pmatrix}.$$

We use again $N = 16$ sites, but now with two fermions (singlet) on every second site for the initial state. In order to compare it with the previous systems we perform simulations

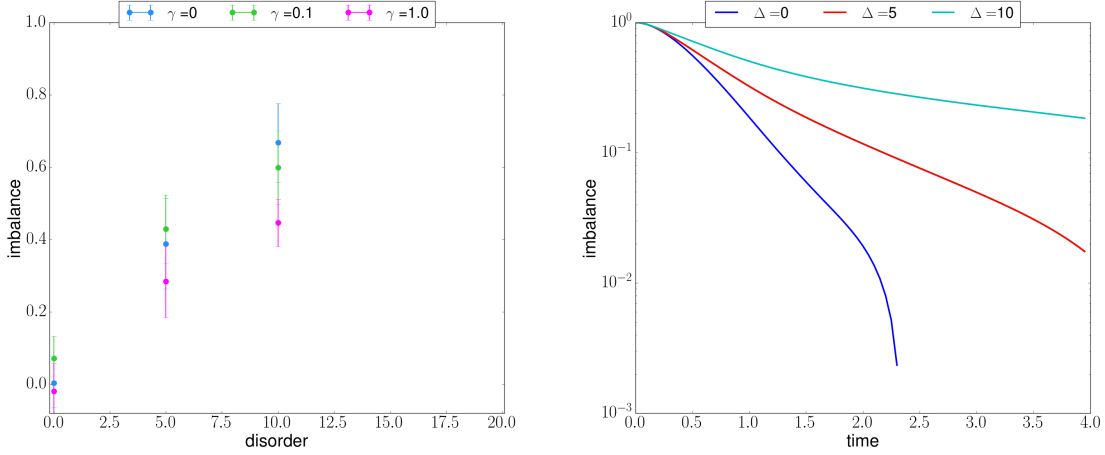


Figure 17: Saturation values and time evolution for the spinful fermionic chain with $N = 16$ sites and with dephasing. The Hamiltonian is described in equation 51 and the Lindblad-operators are similar to equation 40. **Left** The saturation values of the imbalance are shown for low coupling strengths and an interaction strength $U = 1$. Note that we have chosen the disorder range for the plot as before, although, due to lack of time, the simulations for $\Delta = 3$ and $\Delta = 20$ were not performed. The expected memory effects are again clearly visible and the saturation value of the imbalance grows with the disorder strength. Moreover, the dependence on the coupling strength is similar to the one observed for the spinless fermionic chain (see figure 15). **Right** Logarithmic presentation of the time evolution of the imbalance value I for a high coupling strength $\gamma = 10$ and an interaction strength of $U = 1$. We have again no localisation, but an nearly exponential decay of the imbalance value I . However, it is difficult to calculate decay constants λ as described in 3.2.4 on page 22, due to the not completely exponential decay. Nevertheless, we see similar effects for low and for high coupling strengths γ to the spinless case (see 3.2.4 on page 22).

with and without dissipation. For the isolated case ($\gamma = 0$) we use again 400 time steps of $\tau = 0.01$ and we set the Kraus dimension to one and the limit for the bond dimension to 200. In the dissipative case the limit for the Kraus dimension is set to 20 and for the bond dimension to 30. This allows simulations in reasonable time, but leads to greater errors than before (see appendix B on page 33). Nevertheless, the time evolution of the system is very similar to the spinless fermionic chain with dephasing (see 3.2.4 on page 22), because the imbalance saturation values show a similar dependence on the disorder and the coupling to the environment (see figure 17). Moreover, we observe again localisation for small coupling strengths and an nearly exponential decay of the imbalance value for large coupling strengths. With these nicely fitting results the actual error we are making might be much lower than the maximum possible one (see appendix B on page 33). Furthermore, this suggests that the spinless fermionic chain, can be used to simulated the spinful chain to a good extent.

4 Conclusion

In this thesis we have investigated the influence of disorder on open as well as on isolated interacting quantum many-body systems by performing simulations with tensor networks. We have studied one-dimensional fermionic interacting spin chains under the influence of random frozen disorder, which could be coupled to the environment in different ways. Our probe is the particle number difference between sites. To this end we initialise all systems with a charged density wave with particles only on every second site, meaning the imbalance I between even and odd sites is maximal. In case of the isolated spinless fermionic chain we found localisation effects in the presence of disorder, whereby the imbalance saturation values were higher for larger disorder strengths. Our results are in good agreement with the result of the experiment mentioned in section 2.3. By enabling dephasing for this system we still saw this localisation effect persists for small coupling strengths on the time scales considered. For increased coupling strengths the saturation values decreased if all other parameters are fixed. In the extreme case of large coupling parameters all memory of the initial state will be lost eventually and we observed that the imbalance decreases exponentially. For a different coupling to the environment in form of particle loss we again saw similar localisation for small coupling strengths. Moreover, the linear dependence of the decay rate of the particle loss on the coupling strength, as mentioned in the experiment [4], was observed. We also studied spinful fermionic systems which are costlier to simulate, giving much larger error bounds. However, the results showed both in the isolated and coupled cases very similar behaviour to the spinless system, suggesting that the qualitative behaviour is almost independent on the details of the system. From these results we can conjecture that quantum many-body systems with disorder are not stable under influences from the environment, but if these are small enough there might be meta stable states for certain time scales.

To investigate this further, longer simulations are needed, which should also have smaller error bounds. However, this is not easy to achieve due to the unbounded growth of correlations, which are hard to capture with matrix product operators [7]. In addition, one could take the average imbalance value over more realisations in the disorder cases, in order to achieve a better resolution for the saturation values of the imbalance. Moreover, it would be interesting to find and study dissipation models which give rise to meta stable regimes under disorder also for large couplings to the environment. The existence of these has been very recently suggested for the non-interacting case [20].

References

- [1] N. W. Ashcroft and N. Mermin. *Solid State Physics*. Brooks/Cole Cengage Learning, Belmont, 1976.
- [2] P. W. Anderson. Absence of diffusion in certain random lattices. *Phys. Rev.*, 109(5):1492, 1958.
- [3] M. Schreiber, S. S. Hodgman, P. Bordia, H. P. Lüschen, M.H. Fischer, R. Vosk, E. Altman, U. Schneider, and I. Bloch. Observation of many-body localization of interacting fermions in a quasirandom optical lattice. *Science*, 349(6250):842, 2015.
- [4] H. P. Lueschen, P. Bordia, S. S. Hodgman, M. Schreiber, S. Sarkar, A J. Daley, M. H. Fischer, E. Altman, I. Bloch, and U. Schneider. Signatures of many-body localization in a controlled open quantum system. arXiv:1610.01613, 2016.
- [5] M. Friesdorf. *Closed quantum many-body systems out of equilibrium*. Dissertation, Freie Universitaet Berlin, 2016.
- [6] D. A. Huse. Viewpoint: Many-body localization needs a bath. *Physics*, 9(76), 2016.
- [7] J. H. Bardarson, F. Pollmann, and J. E. Moore. Unbounded growth of entanglement in models of many-body localization. *Phys. Rev. Lett.*, 109(1):017202, 2012.
- [8] M. Goihl, M. Friesdorf, A. H. Werner, W. Brown, and J. Eisert. Experimentally accessible witnesses of many-body localisation. arXiv:1601.02666, 2016.
- [9] A. H. Werner, D. Jaschke, P. Silvi, M. Kliesch, T. Calarco, J. Eisert, and S. Montangero. Positive tensor network approach for simulating open quantum many-body systems. *Phys. Rev. Lett.*, 116(23):237201, 2016.
- [10] J. Eisert. Entanglement and tensor network states. *Modeling and Simulation*, 3:520, 2013.
- [11] M. A. Nielsen and I. L. Chuang. *Quantum Computation and Quantum Information*. Cambridge University Press, Cambridge, 10th edition, 2010.
- [12] U. Schollwoeck. The density-matrix renormalization group in the age of matrix product states. *Annals of Physics*, 326(1):96, 2011.

- [13] G. Vidal. Efficient classical simulation of slightly entangled quantum computations. *Phys. Rev. Lett.*, 91(14):147902, 2003.
- [14] M. B. Hastings. An area law for one-dimensional quantum systems. *Journal of Statistical Mechanics: Theory and Experiment*, (08):P08024, 2007.
- [15] J. Eisert, M. Cramer, and M. B. Plenio. *Colloquium: Area laws for the entanglement entropy*. *Rev. Mod. Phys.*, 82(1):277, 2010.
- [16] H. P. Breuer and F. Petruccione. *The Theory of Open Quantum Systems*. Oxford University Press, Oxford, 2002.
- [17] N. Hatano and M. Suzuki. Tensor networks and graphical calculus for open quantum systems. *Lect. Notes Phys.*, 679:37, 2005.
- [18] M. Kliesch, D. Gross, and J. Eisert. Matrix-product operators and states: Np-hardness and undecidability. *Phys. Rev. Lett.*, 113(16):160503, 2014.
- [19] P. Jordan and E. Wigner. Über das paulische äquivalenzverbot. *Zeitschrift für Physik*, 47(9):631, 1928.
- [20] I. Yusipov, T. Laptjeva, S. Denisov, and M. Ivanchenko. Anderson localization in open systems. arXiv:1612.01503, 2016.

A Statistic for the disorder simulations

The imbalance values shown in the main part of this thesis (section 3) are the average over imbalance values for different disorder realisations, whereby we are performing 20 simulations for each different non zero disorder strengths. The necessity for that can be seen in figure 18, where we show an example of 20 different disorder realisations for low and high dissipation. As seen in 3.2.4 on page 22 the influence of the disorder is much higher in case of low coupling strengths $\gamma \leq 1$. This leads to a higher variation in the time evolution of the imbalance value. Because we take the average values this also leads to less oscillations than happen for a fixed realisation. This explains the different shape of the disorder realisations to the one without disorder. However, the described localisation effects are still clearly visible.

Error bars for the saturation values

The error for the saturation values of the imbalance are computed differently for systems with and without disorder. In the case of disorder, we first compute a saturation value for each disorder realisation and for the error the standard deviation is taken. Then the error for the average saturation value is computed with the propagation of uncertainty for mean values. The size of these errors can be more than 10^{-1} (for low coupling strengths). Contrary to that, we perform only one simulation for each different realisation without disorder, due to the lack of randomness. In this case we take the standard deviation for the saturation error.

B Simulation errors

We have two error sources in our simulations. On the one hand, we calculate saturation values and therefore also the averaged imbalance values over 20 different disorder realisations (see appendix A). On the other hand, we are discarding singular values in order to keep the size of our tensor network constant (see 1.4.2 on page 10).

Discarded weight

As discussed in 1.4.2, the magnitude of the discarded weight are saved during the time evolution. This quantity gives a one norm bound for the upper bound error of the simulated time evolution to the true time evolution [9]. We can decompose the total discarded weight into two components, the truncated singular values of the bond dimension and the ones for the Kraus dimension. For the isolated spinless system, where we can use a high threshold for

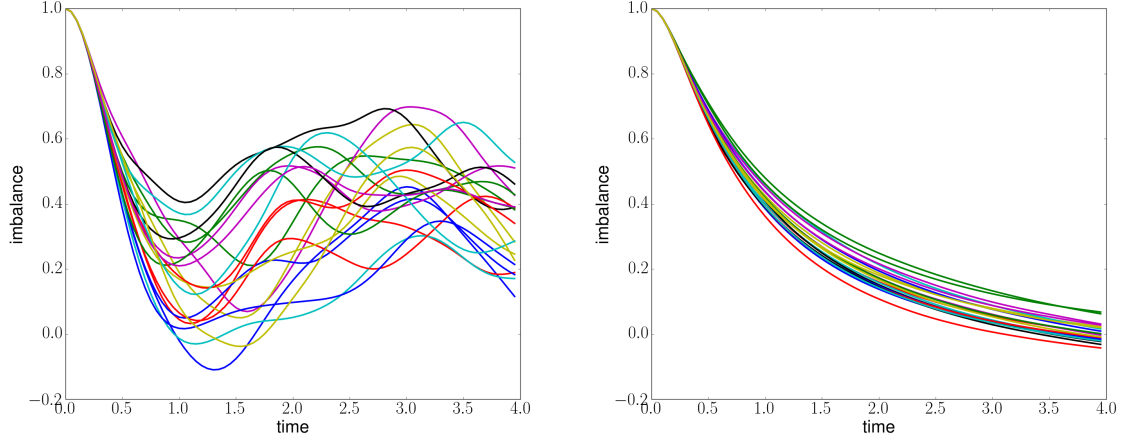


Figure 18: Time evolution for the spinless fermionic chain with $N = 16$ sites and with dephasing. The Hamiltonian is described in equation 39 and the used Lindblad-operators are shown in equation 40. Time dependence of the imbalance I is shown for 20 different disorder realisations for one set of parameters ($\Delta = 3$, $U = 1$). **Left** For a low coupling strength of $\gamma = 0.1$ the different influences of the random disorder realisations are clearly visible. However, all of them show similar localisation. **Right** For a high coupling strength $\gamma = 5$. The different random disorder realisations do not differ much.

the bond dimension, we get a total discarded weight of 10^{-3} for the bond dimension, which is the sum of all discarded weights for all time steps and sites. For the dissipative systems we additionally get a discarded weight for the Kraus dimension. This value, however, varies quite strongly for the different couplings to the environment. The dissipation in form of particle loss (see 3.2.5 on page 25) leads to a much lower discarded weight for the Kraus dimension than for local dephasing. This is the reason for using the threshold 10 for the Kraus dimension, which allows the higher threshold 50 for the bond dimension in order to be able to perform the simulations in a reasonable time, but getting smaller discarded weights. The total discarded weights in this case are of the order 10^{-2} for the bond dimension and 10^{-1} for the Kraus dimension. For similar simulation times the discarded weights for the dephasing simulations are higher: We get total discarded weights of the order $10^1 - 10^2$ for the bond dimension and 10^2 for the Kraus dimension by using a threshold of 30 for both. However, we conjecture that we still get reasonable approximations of the time evolution of the system with respect to the imbalance value, because we can compare with simulations with higher thresholds (as can be seen in figure 19 and figure 20). These show very similar time evolution of the imbalance. In fact, the variations of the imbalance value for our time scales are smaller than $2 \cdot 10^{-2}$. The comparison is done for a medium coupling strength

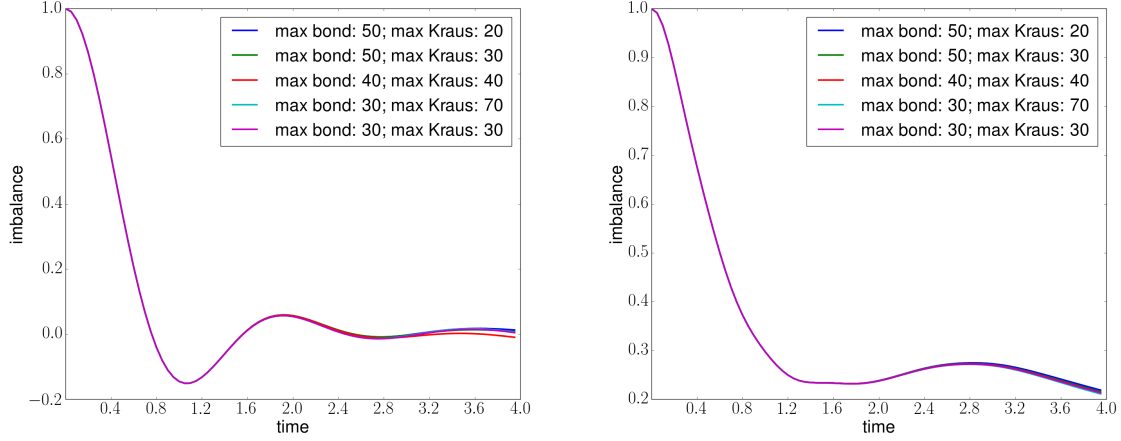


Figure 19: Time evolution for the spinless fermionic chain with $N = 16$ sites and with dephasing for different thresholds of the bond and the Kraus dimension. The Hamiltonian is described in equation 39 and the used Lindblad-operators are shown in equation 40. The interaction strength is set to $U = 1$ and the coupling with the environment to $\gamma = 1$, because the discarded weights are in this case the largest. **Left** The time dependence of the imbalance I is shown for a disorder strength of $\Delta = 0$. **Right** The time dependence of the imbalance I is shown for a disorder strength of $\Delta = 5$. In this case all simulations have the same set of local disorder parameter Δ_i , which are generated randomly in advance.

$\gamma = 1$ and for disorder strengths of $\Delta = 0$ and $\Delta = 5$, because we get the largest errors for these parameter combinations. For other parameter sets we observe a similar behaviour. In order to compare the imbalance values even for the disorder realisation, all simulations have the same set local disorder parameters Δ'_i (see equation 39), which are generated randomly in advance. For these fixed values we perform simulations for different thresholds to the bond and Kraus dimension. This is done for five different disorder realisations and only the one with the largest variations is shown in the figures.

In the case of the spinful fermionic chain with dephasing (see 3.3 on page 27) the errors are even larger, because we have a local dimension of $d = 4$ now. The errors for the bond and the Kraus dimension are now larger than 10^5 . However as seen from the results (see 3.3) this might still lead to a reasonable description of the time evolution of the imbalance. For the isolated spinful fermionic chain we get discarded weights of the order of 10^{-1} .

Overall we can assume that the deviations of the statistic have a greater impact to the imbalance value than the error we are making by discarding singular values.

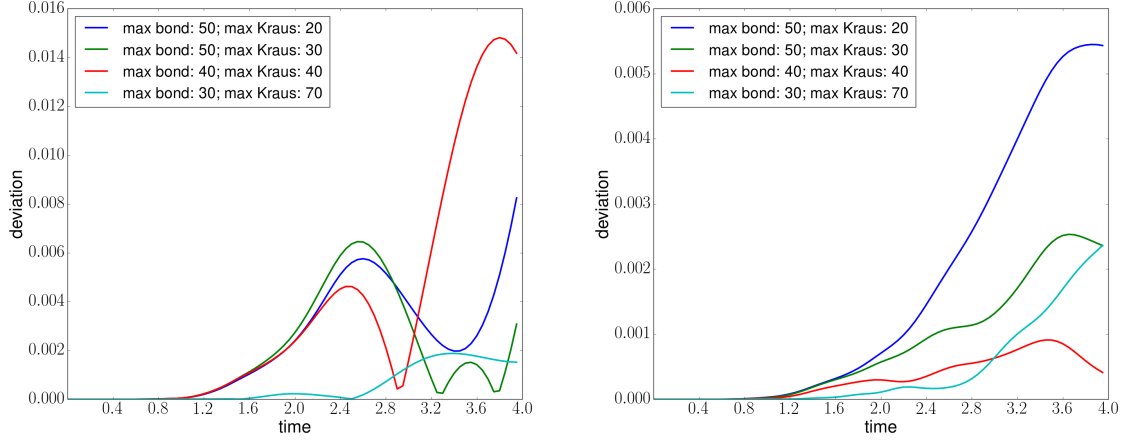


Figure 20: Deviation of simulations for different bond and Kraus dimensions from the simulation with both bond and Kraus dimension 30. The simulation are the ones shown in figure 19. **Left** Deviation of the simulations without disorder. **Right** Deviation of the simulations with disorder.

C Dependence of particle loss on the coupling strength

The coupling in form of particle loss leads to a fast decay of the particle number for high coupling strengths γ , which is a problem for our time scales, because the machine precision gets more important (see 3.2.5 on page 25). However, it is still interesting to study the particle loss rate in the beginning, in order to compare it to the exponential one in the experiment [4] (see 2.3 on page 15). In order to simulate the beginning of our other simulations we perform simulations with 500 time steps of $\tau = 0.001$. The observable is in this case not the imbalance, but the total particle number on the first chain. This is done for the coupling strengths $\gamma = \{1, 5, 10, 20, 50, 100\}$ and the decay of the particle number over time is shown in figure 21. The disorder strength Δ seems not to influence this process at all, because the decay is completely the same for $\Delta = 5$ and $\Delta = 0$. Nevertheless, there could still be a different behaviour for other disorder strenghts. In this semi logarithmic plot the exponential decay is clearly visible, until we reach a very small constant value in some cases. Moreover, the decay constant λ is proportional to the coupling strength γ (see figure 21). Therefore, we see the same linear dependance of the decay rate of the particle number for particle loss to the environment as in the stated experiment (see 2.3 on page 15 [4]) .

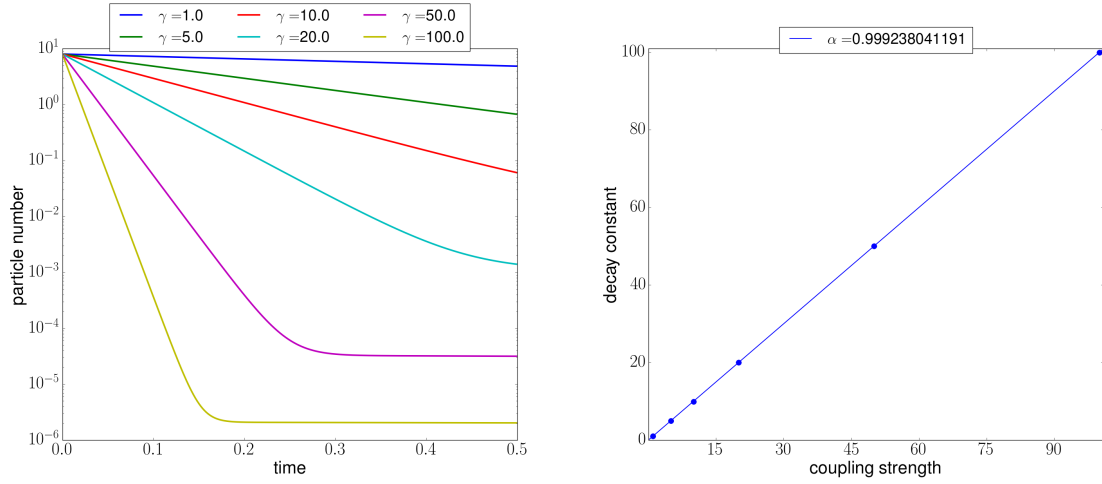


Figure 21: Left Time dependence of the total particle number for the spinless fermionic chain with particle loss. The Hamiltonian is described in equation 45 on page 25 and the used Lindblad-operator is shown in equation 46. The simulations are done for coupling parameters $\gamma = \{1, 5, 10, 20, 50, 100\}$ and for 500 time steps of the magnitude $\tau = 0.001$, meaning we are only simulating the beginning of our other simulations. In this semi-logarithmic plot, the exponential decay is clearly visible until a very small saturation is reached. **Right** The decay constants λ were computed with linear regression and shown with their errors, which are barely visible due to their size. The proportionality (with the factor α) between the decay constant and the coupling strength γ is clearly visible, which was also seen in the experiment (see 2.3 on page 15).